Method for inferring the axis orientation of cylindrical magnetic flux rope based on single-point measurement

Z. J. Rong,[1,2] W. X. Wan,[1,2] C. Shen,[3] T. L. Zhang,[4,5] A. T. Y. Lui,[6] Yuming Wang,[4] M. W. Dunlop,[7] Y. C. Zhang,[3] and Q.-G. Zong[8]

[1]   We develop a new simple method for inferring the orientation of a magnetic flux rope, which is assumed to be a time-independent cylindrically symmetric structure via the direct single-point analysis of magnetic field structure. The model tests demonstrate that, for the cylindrical flux rope regardless of whether it is force-free or not, the method can consistently yield the axis orientation of the flux rope with higher accuracy and stability than the minimum variance analysis of the magnetic field and the Grad-Shafranov reconstruction technique. Moreover, the radial distance to the axis center and the current density can also be estimated consistently. Application to two actual flux transfer events observed by the four satellites of the Cluster mission demonstrates that the method is more appropriate to be used for the inner part of flux rope, which might be closer to the cylindrical structure, showing good agreement with the results obtained from the optimal Grad-Shafranov reconstruction and the least squares technique of Faraday's law, but fails to produce such agreement for the outer satellite that grazes the flux rope. Therefore, the method must be used with caution.

1. Introduction

[2] A magnetic flux rope is a structure with magnetic field lines (MFLs) wrapping and rotating around a central axis to form a helical magnetic structure [e.g., *Hones*, 1977; *Hones et al.*, 1982; *Hughes and Sibeck*, 1987]. It is generally considered as a product of magnetic reconnection in the eruptive energy processes, e.g., magnetospheric substorm [e.g., *Schindler*, 1974; *Moldwin, and Hughes*, 1993; *Nagai et al.*, 1994; *Lee,* 1995; *Lin et al.*, 2008; *Gekelman et al.*, 2012]. It is observed ubiquitously in space plasma environment, e.g., in Earth's (magnetized planet) magnetotail [e.g., *Slavin et al.*, 2003; *Zong et al.*, 1997, 2004; *Zhang et al.*, 2007], and in the Venus (unmagnetized planet) induced magnetotail [*Zhang et al.*, 2012], in the cusp region [e.g., *Zong et al.*, 2003], in magnetopause as flux transfer events (FTEs) [e.g., *Russell and Elphic*, 1979a; *Lockwood and Hapgood*, 1998; *Slavin et al.*, 2009], in solar wind as magnetic cloud [e.g., *Burlaga*, 1988; *Lepping et al.*, 1990], even in the ionosphere of unmagnetized planet [e.g., *Russell and Elphic*, 1979b; *Vignes et al.*, 2004; *Wei et al.*, 2010].

[3] Accurate estimation of the axis orientation of a flux rope is vital in studies of its origin and evolution, as well as in exploring the dynamics of magnetic reconnection. However, this issue is still not well resolved.

[4] Currently, the most widely used single-point method to infer the axis orientation of a flux rope is the minimum variance analysis of magnetic field (BMVA) [*Sonnerup and Cahill*, 1968], which was originally developed to analyze the orientation of plasma discontinuity with the yielded three orthogonal eigen directions, i.e., **L** (maximum variance direction) , **M** (intermediate variance direction), and **N** (minimum variance direction). However, actual application demonstrates that, depending critically on the spacecraft (S/C) path and the magnetic field structure, any of the three eigen directions of BMVA is fairly close to the actual axis orientation [e.g., *Moldwin and Hughes*, 1991; *Xiao et al.*, 2004; *Pu et al.*, 2004]. To avoid the uncertainties of BMVA, the method using the current density instead of magnetic field to perform

[1]CAS Key Laboratory of Ionospheric Environment, Institute of Geology and Geophysics, Chinese Academy of Sciences, Beijing, China.

[2]Beijing National Observatory of Space Environment, Institute of Geology and Geophysics, Chinese Academy of Sciences, Beijing, China.

[3]State Key Laboratory of Space Weather, Center for Space Science and Applied Research, Chinese Academy of Sciences, Beijing, China.

[4]Key Laboratory of Basic Plasma Physics, Department of Geophysics and Planetary Sciences, University of Science and Technology of China, Hefei, China.

[5]Space Research Institute, Austrian Academy of Sciences, Graz, Austria.

[6]Applied Physics Laboratory, Johns Hopkins University, Laurel, Maryland, USA.

[7]Rutherford Appleton Laboratory, Chilton, DIDCOT, Oxfordshire, UK.

[8]Department of Geophysics, Peking University, Beijing, China.

Corresponding author: Z. J. Rong, CAS Key Laboratory of Ionospheric Environment, Institute of Geology and Geophysics, Chinese Academy of Sciences, Beijing, 100029, China. (rongzhaojin@mail.iggcas.ac.cn)
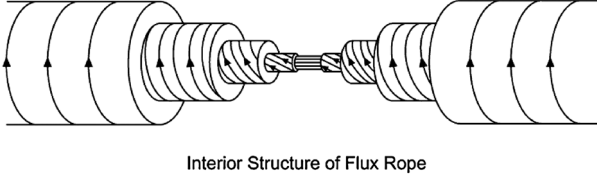
Figure 1. The interior structure of flux rope (adapted with permission from *Russell and Elphic* [1979b]).

minimum variance analysis (MVA) is suggested to be a better choice [*Xiao et al.*, 2004; *Pu et al.*, 2004]. Some researchers argued that performing MVA on the unit magnetic vector (bMVA), i.e., $\hat{\mathbf{b}}\,(\mathbf{B}/|\mathbf{B}|)$, can yield more reasonable results than that of BMVA [e.g., *Lepping et al.*, 1990; *Gulisano et al.*, 2007].

[5] Besides minimum variance analysis, fitting methods [e.g., *Burlaga*, 1988; *Burlaga et al.*, 1990; *Lepping et al.*, 1990; *Wang et al.*, 2002, 2003; *Slavin et al.*, 2003; *Zhang et al.*, 2008] also have been used for the orientation analysis based on the force-free field models. However, one cannot assure that the detected structure of a flux rope always fits well with the force-free model.

[6] Some methods based on the physical laws are also presented. For example, the Grad-Shafranov (GS) reconstruction method developed recently [*Hau and Sonnerup*, 1999; *Hu and Sonnerup*, 2002] can yield the axis orientation of flux rope and recover the optimal map of field distribution in the cross-section by solving the GS equation. However, a trial and error scheme is needed to search for the axis orientation, for which the total transverse pressure $p + \left(\frac{\mathbf{B}_z^2}{2\mu_0}\right)$ versus magnetic potential function A displays minimum scatter. The multispacecraft GS technique [*Sonnerup et al.*, 2004; *Hasegawa et al.*, 2005] may yield a better resolution than the single-spacecraft GS technique. The resulting optimal map, however, no longer obeys the GS equation precisely. According to the GS reconstruction techniques, *Li et al.* [2009] also have introduced a flux rope orientation inferring techniques with the residue defined by field invariants for a specified flux rope model. *Sonnerup and Hasegawa* [2005] presented a least squares technique for the determination of axis orientation based on the Faraday's law, $\nabla \times \mathbf{E} = -\,\partial\mathbf{B}/\partial t = 0$, which, under the assumption of time-independent flux rope with a 2-dimensional structure, requires the intrinsic axial electric field, E_z, to be constant in space and time.

[7] Based on the multipoint measurements of Cluster tetrahedron, some multipoint analysis methods are presented [e.g., *Shi et al.*, 2005; *Zhou et al.*, 2006; *Shen et al.*, 2007], where the derived higher order physical quantities, e.g., the direction of magnetic field gradient [*Zhou et al.*, 2006], the characteristic directions of magnetic field spatial variation [*Shi et al.*, 2005; *Shen et al.*, 2007], etc., are the key parameters to infer the orientations of flux rope. The validity of those methods requires the size of the Cluster constellation to be much smaller than the typical size of flux rope; otherwise, the assumption of linear variation would result in comparable errors.

[8] Although the currently known single-point methods can afford a possible way to infer the axis orientation, the method that is based on the direct analysis of MFLs'

geometric structure to infer the orientation is still unavailable. Meanwhile, in contrast to the multipoint analysis of the Cluster mission, most current satellite missions do not have the unique multisatellite configuration like Cluster and thus rely on single-point method for flux rope analysis. For this reason, it is useful to improve the single-point method based on the direct analysis of field geometric structure, which is the main goal of this research.

[9] In the following, based on the assumption of cylindrical symmetry, the theory of the method is presented first. Then, to demonstrate the accuracy and practicability of the new method, model tests and application to true cases are carried out to compare with some known methods. The yielded results demonstrate that our method is reasonable and applicable, but should be used with caution.

2. Approach

2.1. Method Assumptions

[10] Considering the loop-like magnetic structure of the flux rope, it is convenient to adopt the cylindrical coordinates $\{\hat{\mathbf{r}}, \hat{\boldsymbol{\varphi}}, \hat{\mathbf{z}}\}$ for orientation analysis, where $\hat{\mathbf{r}}$, $\hat{\boldsymbol{\varphi}}$ and $\hat{\mathbf{z}}$ are referred to as the unit vector of radial, azimuth, and axis direction, respectively. As shown in Figure 1, one well-known model is the model of cylindrical force-free field (($\nabla \times \mathbf{B}$) × $\mathbf{B} = 0$). However, the actual detected flux rope is generally variable and complicated, e.g., some may have two-dimensional closed loop field structure, while others may have a flux rope embedding in the outer closed loop field [*Zong et al.*, 2004], and it may not be force-free field [e.g., *Slavin et al.*, 2003; *Lui et al.*, 2007]. Thus, to simplify the study and relax the confinement of force-free field, some reasonable assumptions need to be made as stated below:

1. The magnetic field lines of a flux rope rotate about a common axis forming a spiral structure. The axis is in a fixed direction during the passage of S/C.
2. The spacecraft trajectory across the flux ropes is straight, so that the unit direction of relative velocity $\hat{\mathbf{v}}$ ($\hat{\mathbf{v}} = \mathbf{V}/V$) to flux rope is constant, and the spatial position along the trajectory can be computed by integrating $V(t)$.
3. The magnetic structure is stable and unchanged during the passage of S/C; the flux rope is an ideal cylindrical symmetry, the magnetic field strength, B, is independent of the coordinate φ and z, i.e., $\left(\frac{\partial}{\partial t}, \frac{\partial}{\partial \varphi}, \frac{\partial}{\partial z}\right)B = 0$.

[11] The known data are the single-point measurement of magnetic field vector and the relative velocity of S/C to flux rope. Hence, the key issue is how to use these known data to infer the axis orientation of flux rope.

2.2. Method

[12] The helical MFLs of flux rope have their intrinsic handedness of helicity. As shown in Figure 2, the handedness of MFLs is of right-hand if the current density is parallel to the axis field, which points out of the page (Figure 2a), while it is of left-hand if the current density is antiparallel (Figure 2b). The unit direction of magnetic field, $\hat{\mathbf{b}}$ ($\hat{\mathbf{b}} = \mathbf{B}/B$) and the unit direction of relative velocity, $\hat{\mathbf{v}}$ ($\hat{\mathbf{v}} = \mathbf{V}/V$) comprise two components, i.e., the parallel components $\mathbf{b}_{\parallel}$, $\mathbf{v}_{\parallel}$ and perpendicular components $\mathbf{b}_{\perp}$, $\mathbf{v}_{\perp}$, being parallel and perpendicular to the

a

b

Right-hand
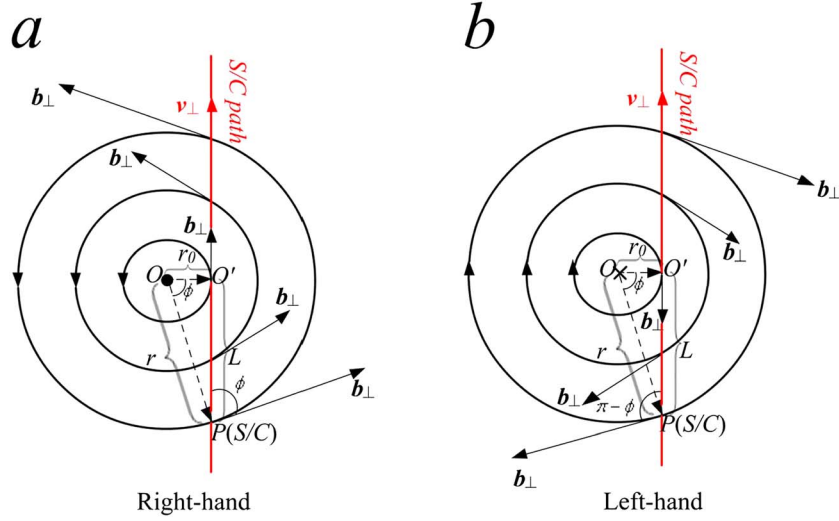
Left-hand

Figure 2. Sketched diagram to show the helical handedness of flux rope and the variation of field direction along the path of S/C on the cross-section. (a) The right-handed structure. (b) The left-handed structure. The red arrow is the projection of S/C path, while the black arrow is the perpendicular direction of unit magnetic field vector to the axis orientation.

axis orientation, respectively. As sketched in Figure 2 in the projection of cross-section, no matter what the helical handedness is, $\mathbf{b}_\perp$ would be parallel or antiparallel to $\mathbf{v}_\perp$ at the innermost of the flux rope (O' point), so that the product of $\mathbf{v}_\perp \cdot \mathbf{b}_\perp / v_\perp b_\perp$ would reach the extreme at the innermost. One question is naturally raised: does the product of $\hat{\mathbf{v}} \cdot \hat{\mathbf{b}}$ also reach the extreme at the innermost along the path? If it indeed does, the innermost location can be identified by checking $\hat{\mathbf{v}} \cdot \hat{\mathbf{b}}$ timing series, and the axis orientation should lie in the plane constituted by $\hat{\mathbf{v}}$ and $\hat{\mathbf{b}}$, which is then the unit magnetic vector in the innermost location. Thus, along the path of S/C, it is worth checking the variation of $\hat{\mathbf{v}} \cdot \hat{\mathbf{b}}$, which is expressed as

$$\hat{\mathbf{v}} \cdot \hat{\mathbf{b}} = \mathbf{v}_\parallel \cdot \mathbf{b}_\parallel + \mathbf{v}_\perp \cdot \mathbf{b}_\perp = v_\parallel b\cos\theta + v_\perp b\sin\theta\cos\phi, \quad (1)$$

where, θ is the angle between the axis orientation and the local magnetic vector, ϕ is the angle between $\mathbf{v}_\perp$ and $\mathbf{b}_\perp$, b is the unit scalar of $\hat{\mathbf{b}}$ ($b = 1$). Particularly, for the ideal closed loop field structure ($\theta = 90°$), $\mathbf{b}_\parallel = 0$, the term $\hat{\mathbf{v}} \cdot \hat{\mathbf{b}} = \mathbf{v}_\perp \cos\phi$ will reach the extreme at the innermost location. However, generally, θ and ϕ vary simultaneously along the S/C path, that is, θ and ϕ are functions of the distance to the innermost position, L, along the path in the cross-section (see Figure 2).

[13] We should recall that, because $\hat{\mathbf{v}}$ has been assumed to be constant, the parallel component $\mathbf{v}_\parallel$ and perpendicular component $\mathbf{v}_\perp$ are supposed to be constant accordingly. Taking the partial derivative of L at both sides of equation (1) and considering $b = 1$, we can get

$$\frac{\partial}{\partial L} \hat{\mathbf{v}} \cdot \hat{\mathbf{b}} = -v_{//}\sin\theta\frac{\partial\theta}{\partial r}\frac{\partial r}{\partial L} + v_\perp\cos\theta\frac{\partial\theta}{\partial r}\frac{\partial r}{\partial L}\cos\phi$$
$$- v_\perp\sin\theta\sin\phi\frac{\partial\phi}{\partial r}\frac{\partial r}{\partial L}. \quad (2)$$

[14] At the innermost location, the radial direction $\hat{\mathbf{r}}$ is perpendicular to $\mathbf{v}_\perp$ (see Figure 2), i.e., $(\frac{\partial r}{\partial L}) \sim 0$; meanwhile, ϕ is 0° or 180° there. Therefore, all the three terms on the right side of equation (2) equal to zero, which

means $\hat{\mathbf{v}} \cdot \hat{\mathbf{b}}$ would reach the extreme in the innermost location along the path.

[15] Therefore, by checking the plot of $\hat{\mathbf{v}} \cdot \hat{\mathbf{b}}$ along the path, the time when S/C is in the innermost location can be identified. The corresponding $\hat{\mathbf{b}}$ at that time is indicated as $\hat{\mathbf{b}}_{in}$. Because $\hat{\mathbf{b}}_{in\perp}$ and $\hat{\mathbf{v}}_\perp$ are toward the same direction at that time, so, the axis orientation should lie in the plane that formed by the $\hat{\mathbf{v}}$ and $\hat{\mathbf{b}}_{in}$, i.e., the actual axis orientation $\hat{\mathbf{n}}$, the magnetic field direction at the innermost $\hat{\mathbf{b}}_{in}$, and the direction of relative velocity $\hat{\mathbf{v}}$ are coplanar, as sketched in Figure 3. Therefore, one direction perpendicular to the axis orientation can be determined by $\hat{\mathbf{e}}_1 = \frac{\hat{\mathbf{v}} \times \hat{\mathbf{b}}_{in}}{|\hat{\mathbf{v}} \times \hat{\mathbf{b}}_{in}|}$, and we may define it as one minor orientation.

[16] As shown in Figure 3, we may construct an orthogonal coordinate system $\{\hat{\mathbf{e}}_1, \hat{\mathbf{v}}, , \hat{\mathbf{n}}_0\}$, where $\hat{\mathbf{n}}_0 = \hat{\mathbf{e}}_1 \times \hat{\mathbf{v}}$. In
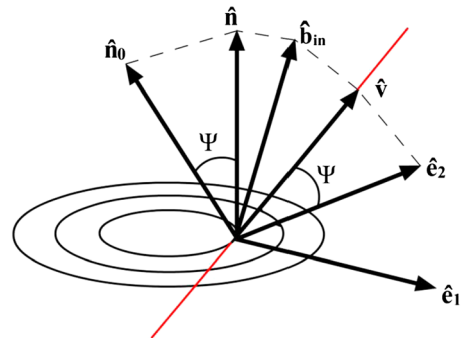
Figure 3. The geometric relationship between $\hat{\mathbf{n}}_0$, $\hat{\mathbf{n}}$, $\hat{\mathbf{b}}_{in}$, $\hat{\mathbf{v}}$, $\hat{\mathbf{e}}_2$, and $\hat{\mathbf{e}}_1$ at the innermost location along the path (red line). Note, all the unit vectors are coplanar (end of arrows are connected with dashed lines) except for $\hat{\mathbf{e}}_1$. $\hat{\mathbf{n}}_0$, $\hat{\mathbf{v}}$, and $\hat{\mathbf{e}}_1$ constitute an orthogonal system satisfying $\hat{\mathbf{n}}_0 = \hat{\mathbf{e}}_1 \times \hat{\mathbf{v}}$, while $\hat{\mathbf{n}}$, $\hat{\mathbf{e}}_2$ and $\hat{\mathbf{e}}_1$ also constitute an orthogonal system satisfying with $\hat{\mathbf{n}} = \hat{\mathbf{e}}_1 \times \hat{\mathbf{e}}_2$. The angle between $\hat{\mathbf{n}}_0$ and $\hat{\mathbf{n}}$ is defined as Ψ.

such coordinates, the actual axis orientation $\hat{\mathbf{n}}$ and the other minor orientation $\hat{\mathbf{e}}_2$ can be expressed as

$$\begin{cases} \hat{\mathbf{e}}_2 = -\hat{\mathbf{n}}_0\sin\Psi + \hat{\mathbf{v}}\cos\Psi \\ \hat{\mathbf{n}} = \hat{\mathbf{n}}_0\cos\Psi + \hat{\mathbf{v}}\sin\Psi \\ \hat{\mathbf{n}} = \hat{\mathbf{e}}_1 \times \hat{\mathbf{e}}_2 \end{cases}, \qquad (3)$$

where, Ψ is the angle between $\hat{\mathbf{n}}_0$ and $\hat{\mathbf{n}}$. Obviously, if Ψ is known, then $\hat{\mathbf{n}}$ and $\hat{\mathbf{e}}_2$ can be derived from equation (3). To achieve this task, we would reexamine the sketched diagram in Figure 2.

[17] From Figure 2, along a given path, at time of t_i, the position of S/C is at P point. While at the time of t_{in}, S/C is in the innermost location (O' point) with the distance to the axis center (O point) being r_0 defined as the impact distance. The relative spatial vector pointing from P to O' is $\vec{PO'} = \mathbf{V}\Delta t_i$, where $\Delta t_i = t_{in} - t_i$. It should be noted that, if the impact distance at time of t_i can be evaluated as r_{0i}, then the evaluated impact distance should keep constant along the path for the ideal cylindrical symmetry type. In view of this, we may construct a residue equation as

$$\sigma^2 = \frac{1}{M}\sum_{i=1}^{M}(r_{0i} - \langle r_0 \rangle)^2, \qquad (4)$$

where M is the number of data points, and $\langle r_0 \rangle = \frac{1}{M}\sum_{i=1}^{M}r_{0i}$.

[18] From Figure 2, the impact distance can be calculated by

$$r_{0i} = L_i/\tan\phi_i \qquad (5)$$

at time t_i. Where ϕ_i is the angle between $\vec{PO'}$ and $\vec{OO'}$, and L_i is the distance of P to O' in the cross-section, which can be expressed as

$$L_i = \left|\vec{PO'}_\perp\right| = \left|\vec{PO'} - (\vec{PO'}\cdot\hat{\mathbf{n}})\hat{\mathbf{n}}\right|. \qquad (6)$$

[19] For the case of Figure 2a, at time t_i, supposing a flux rope with a circular symmetry, ϕ_i equals the angle between $\mathbf{b}_{i\perp}$ and $\mathbf{v}_\perp$, and can be derived as

$$\cos\phi_i = \frac{\mathbf{b}_{i\perp}\cdot\mathbf{v}_\perp}{|\mathbf{b}_{i\perp}||\mathbf{v}_\perp|} = \frac{\hat{\mathbf{b}}_i\cdot\hat{\mathbf{v}} - (\hat{\mathbf{b}}_i\cdot\hat{\mathbf{n}})(\hat{\mathbf{v}}\cdot\hat{\mathbf{n}})}{|\hat{\mathbf{b}}_i - (\hat{\mathbf{b}}_i\cdot\hat{\mathbf{n}})\hat{\mathbf{n}}||\hat{\mathbf{v}} - (\hat{\mathbf{v}}\cdot\hat{\mathbf{n}})\hat{\mathbf{n}}|},$$
$$\phi_i = \cos^{-1}\left[\frac{\hat{\mathbf{b}}_i\cdot\hat{\mathbf{v}} - (\hat{\mathbf{v}}\cdot\hat{\mathbf{n}})(\hat{\mathbf{b}}_i\cdot\hat{\mathbf{n}})}{|\hat{\mathbf{b}}_i - (\hat{\mathbf{b}}_i\cdot\hat{\mathbf{n}})\hat{\mathbf{n}}||\hat{\mathbf{v}} - (\hat{\mathbf{v}}\cdot\hat{\mathbf{n}})\hat{\mathbf{n}}|}\right]. \qquad (7)$$

[20] For the case of Figure 2b, we can similarly get

$$\cos(\pi - \phi_i) = \frac{\mathbf{b}_{i\perp}\cdot\mathbf{v}_\perp}{|\mathbf{b}_{i\perp}||\mathbf{v}_\perp|},$$
$$\phi_i = \pi - \cos^{-1}\left[\frac{\hat{\mathbf{b}}_i\cdot\hat{\mathbf{v}} - (\hat{\mathbf{v}}\cdot\hat{\mathbf{n}})(\hat{\mathbf{b}}_i\cdot\hat{\mathbf{n}})}{|\hat{\mathbf{b}}_i - (\hat{\mathbf{b}}_i\cdot\hat{\mathbf{n}})\hat{\mathbf{n}}||\hat{\mathbf{v}} - (\hat{\mathbf{v}}\cdot\hat{\mathbf{n}})\hat{\mathbf{n}}|}\right]. \qquad (8)$$

[21] Combining equations (6)–(8), equation (5) can be expanded as

$$r_{0i} = \Delta t_i\left|\mathbf{V} - (\mathbf{V}\cdot\hat{\mathbf{n}})\hat{\mathbf{n}}\right|\left|\tan\left\{\cos^{-1}\left[\frac{\hat{\mathbf{b}}_i\cdot\hat{\mathbf{v}} - (\hat{\mathbf{v}}\cdot\hat{\mathbf{n}})(\hat{\mathbf{b}}_i\cdot\hat{\mathbf{n}})}{|\hat{\mathbf{b}}_i - (\hat{\mathbf{b}}_i\cdot\hat{\mathbf{n}})\hat{\mathbf{n}}||\hat{\mathbf{v}} - (\hat{\mathbf{v}}\cdot\hat{\mathbf{n}})\hat{\mathbf{n}}|}\right]\right\}^{-1}\right|. \qquad (9)$$

[22] Because the axis orientation $\hat{\mathbf{n}}$ is a function of Ψ (see equation (3)), so σ^2 is also a function of Ψ. Thus, the axis orientation $\hat{\mathbf{n}}$ can be calculated numerically by making σ^2 reach the minimum σ_m^2. One should note that, at the time of t_{in}, i.e., when S/C is just at the innermost location, the numerator and denominator of equation (5) are zero. Equation (5) becomes indeterminate. So the data at time of t_{in} should be skipped when computing equation (4).

[23] Through the numerical calculation, two directions of axis orientation are obtained. They are antiparallel to each other. In view of this, we would like to choose the direction which basically points along the $\hat{\mathbf{b}}_{in}$ as the axis orientation, and we may define it as

$$\hat{\mathbf{N}} = sig(\hat{\mathbf{b}}_{in}\cdot\hat{\mathbf{n}})\hat{\mathbf{n}}. \qquad (10)$$

[24] Therefore, $\hat{\mathbf{e}}_2$ can be further yielded accordingly as $\hat{\mathbf{e}}_2 = \hat{\mathbf{N}} \times \hat{\mathbf{e}}_1$. It should note that, here, the meaning of $\hat{\mathbf{N}}$ is different from that of $\mathbf{N}$ as referred in the MVA method (see section 1).

[25] Now that the axis orientation is inferred, the parallel component and azimuthal or perpendicular component of field can be obtained as

$$\mathbf{B}_z = (\mathbf{B}\cdot\hat{\mathbf{N}})\hat{\mathbf{N}}, \mathbf{B}_\varphi = \mathbf{B} - (\mathbf{B}\cdot\hat{\mathbf{N}})\hat{\mathbf{N}}. \qquad (11)$$

[26] With equations (5)–(6), the local distance of S/C to the axis center can be derived as

$$r_i = \sqrt{L_i^2 + \langle r_0 \rangle^2}. \qquad (12)$$

[27] Furthermore, considering $\nabla \times \mathbf{B} = \mu_0\mathbf{j}$, $\partial/\partial z = 0$, $\partial/\partial\varphi = 0$, the parallel and perpendicular or azimuthal current density can be derived as

$$j_{//} = \mu_0^{-1}r^{-1}\frac{\partial(rB_\varphi)}{\partial r}, j_\perp = -\mu_0^{-1}\frac{\partial B_z}{\partial r}. \qquad (13)$$

[28] From equation (12), $\partial r \approx r_{i+1} - r_i$. Therefore, by combining equations (11) and (12), the current density can be numerically calculated via equation (13).

2.3. Summary of Method

[29] Accordingly to the above analysis, the steps of the new method to infer the orientations of flux rope can be summarized as follows:

1. Checking the time series of $\hat{\mathbf{v}}\cdot\hat{\mathbf{b}}$ to find the time t_{in} when $\hat{\mathbf{v}}\cdot\hat{\mathbf{b}}$ reaches the extreme, and the corresponding unit magnetic vector $\hat{\mathbf{b}}_{in}$. Therefore, one direction perpendicular to the axis orientation can be determined by $\hat{\mathbf{e}}_1 = \frac{\hat{\mathbf{v}}\times\hat{\mathbf{b}}_{in}}{|\hat{\mathbf{v}}\times\hat{\mathbf{b}}_{in}|}$.

2. Constructing an orthogonal coordinates $\{\hat{\mathbf{e}}_1, \hat{\mathbf{v}}, \hat{\mathbf{n}}_0\}$ where $\hat{\mathbf{n}}_0 = \hat{\mathbf{e}}_1 \times \hat{\mathbf{v}}$. In such coordinates, the actual axis orientation $\hat{\mathbf{n}}$ and the other perpendicular orientation $\hat{\mathbf{e}}_2$ can be expressed as $\hat{\mathbf{n}} = \hat{\mathbf{n}}_0\cos\Psi + \hat{\mathbf{v}}\sin\Psi$ and $\hat{\mathbf{e}}_2 = -\hat{\mathbf{n}}_0\sin\Psi + \hat{\mathbf{v}}\cos\Psi$, where Ψ is the angle between $\hat{\mathbf{n}}_0$ and $\hat{\mathbf{n}}$
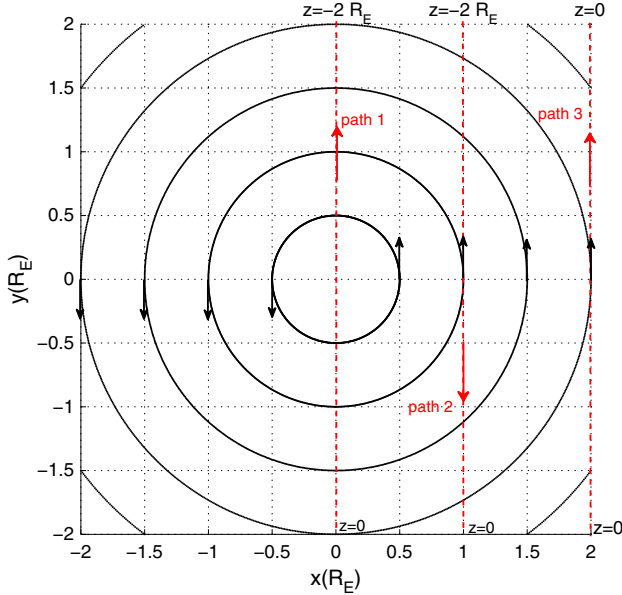
Figure 4. Three different S/C paths relative to the cylindrical flux rope (red dashed lines) are shown on the projected cross-section. Black circle is the projection of MFLs. R_E is the unit of Earth radius.

3. Constructing a residue equation as $\sigma^2(\Psi) = \frac{1}{M}\sum_{i=1}^{M}(r_{0i} - \langle r_0 \rangle)^2$ (see equations (4)–(9), where M is the number of data points, r_{0i} is the inferred impact distance (the closest distance of the path to the axis center), and $\langle r_0 \rangle = \frac{1}{M}\sum_{i=1}^{M}r_{0i}$

4. Numerical adjustment of Ψ making residue function $\sigma^2(\Psi)$ minimum to find the final axis orientation, $\hat{\mathbf{N}}$, which basically points along $\hat{\mathbf{b}}_{in}$, and also find the radial distance to the axis center, r_i, from equation (12).

3. Model Test

[30] To check the accuracy and validity of the method, two classic cylindrically symmetric models of flux rope have been tested along three different paths as shown in Figure 4. For path 1, the location of S/C is linearly varied from ($x=0$, $y=-2$, $z=0$) R_E to ($x=0$, $y=2$, $z=-2$) R_E. For path 2, it is linearly varied from ($x=1$, $y=2$, $z=0$) R_E to ($x=1$, $y=-2$, $z=-2$) R_E. While, for path 3, it varies from ($x=2$, $y=-2$, $z=0$) R_E to ($x=2$, $y=2$, $z=0$) R_E. Thus, the unit direction of relative velocity for the path 1, path 2, and path 3 are $\hat{\mathbf{v}}_1(0, 0.8944, -0.4472)$, $\hat{\mathbf{v}}_2(0, -0.8944, -0.4472)$, and $\hat{\mathbf{v}}_3(0, 1, 0)$, respectively. The Y-component of relative velocity, V_y, for all the three paths are assumed to be constant as 0.2 R_E /s. Therefore, the time interval for the three paths is 20 s, and the relative velocity of S/C for path 1, path 2, and path 3 are $V_1 = V_2 = 0.2239$ R_E/s, $V_3 = 0.2$ R_E/s, respectively. The recorded data resolution is 1 s.

[31] The two tested classic models are:

1. Lundquist-Lepping (L-L) Model [*Lundquist*, 1950]

[32] This model is one specific solution of force-free field $\nabla \times B = \alpha B$ with the assumption of cylindrical symmetry, which can be expressed as

$$B_z = B_0 J_0(\alpha r), B_\varphi = B_0 J_1(\alpha r). \tag{14}$$

[33] For the test, we arbitrarily adopt $B_0 = 2$ nT, $\alpha = R_E^{-1}$.

2. Elphic and Russell (E-R) Model [*Elphic and Russell*, 1983; *Russell*, 1990]

[34] This non-force-free model was constructed with an intense core field inside

$$\begin{cases} B_z = B(r)\cos(\alpha(r)) \\ B_\varphi = B(r)\sin(\alpha(r)) \\ B(r) = B_0\exp(-r^2/b^2) \\ \alpha(r) = \pi/2(1 - \exp(-r^2/a^2)) \end{cases} \tag{15}$$

[35] For the test, $a = R_E$, $b = R_E$, $B_0 = 10$ nT are arbitrarily adopted.

[36] As a comparison, the technique of BMVA [*Sonnerup and Cahill*, 1968], bMVA [e.g., *Lepping et al.*, 1990; *Gulisano et al.*, 2007], and GS reconstruction [*Hu and Sonnerup*, 2002] are also used (see section 1). For the GS reconstruction, the axis orientation is the direction, for which the total transverse pressure P_t versus magnetic potential function A displays minimum scatter. Here $P_t = p + \left(\frac{B_z^2}{2\mu_0}\right)$, p is plasma pressure and $\frac{B_z^2}{2\mu_0}$ is the axis component of magnetic pressure. Because the plasma data are unavailable from both flux rope magnetic field models, we can take $P_t = \left(\frac{B_z^2}{2\mu_0}\right)$ for the GS reconstruction of the L-L model because the plasma pressure force is ignorable for force-free field, but it cannot be done similarly for the non-force-free E-R model. For the E-R model, based on the equilibrium equation $\nabla p = \mathbf{j} \times \mathbf{B} = -\left\{\frac{\nabla B^2}{2\mu_0}\right\} + \{[(\mathbf{B} \cdot \nabla)\mathbf{B}]/\mu_0\}$, and noticing that the gradient direction is radial, one can obtain the plasma pressure as $p = \left(\frac{-B^2}{2\mu_0}\right) - \int\left(\frac{B_\varphi^2}{r\mu_0}\right)dr$. Because the explicit integral expression could not be found, the plasma pressure needs to be numerically calculated for the GS reconstruction application. The results yielded from these methods for both models are arranged in Table 1. Evidently from Table 1, being independent of S/C path in both models, our method can consistently yield the correct axis orientation as the model demanded. In contrast, being strongly dependent on the S/C path, the axis orientations yielded by the technique of BMVA, bMVA, and the GS reconstruction are unstable. Particularly, either of the eigen directions $\mathbf{L}$, $\mathbf{M}$, and $\mathbf{N}$ yielded by BMVA or bMVA is fairly close to the actual axis orientation.

[37] Apart from the analysis of axis orientation, the impact distance of the path at a given time can be found from equation (9). Figure 5 shows the time series of inferred impact distance of the three paths for both models. It is clear that the inferred impact distance for a given path always keeps constant showing good agreement with the known crossing conditions. One should note that due to the singularity at the time of 10 s when S/C are just in the innermost location, the data at that time have been skipped, leading to a gap of impact distance found at that time. Because the impact distance can be estimated accurately, accordingly, the local radial distance and current density have

Table 1. Comparison of Axis Orientations Yielded From BMVA, GS Reconnection and Our Method

Method/ Model	Path	BMVA	bMVA	GS Reconstruction[a]	Our Method
L-L	1	**L** (–1, 0, 0) **M** (0, 0, 1) **N** (0, 1, 0)	**L** (1, 0, 0) **M** (0, 0, 1) **N** (0, –1, 0)	(–0.0872, 0, 0.9962)	(0,0,1)
	2	**L** (–1, 0, 0) **M** (0, 0.2740,0.9617) **N** (0, 0.9617, –0.2740)	**L** (–1, 0, 0) **M** (0, 0.0767,0.9971) **N** (0,0.9971, –0.0767)	(–0.3420, 0, 0.9397)	(0,0,1)
	3	**L** (–1, 0, 0) **M** (0, 0.5682, 0.8229) **N** (0, 0.8229, –0.5682)	**L** (–1, 0, 0) **M** (0,0.3376,0.9413) **N** (0,0.9413,–0.3376)	(–0.6428, 0, 0.7660)	(0,0,1)
E-R	1	**L** (0, 0, 1) **M** (1,0, 0) **N** (0,–1, 0)	**L** (1, 0, 0) **M** (0, 0, 1) **N** (0,–1, 0)	(0.1548, 0.1624, 0.9745)	(0,0,1)
	2	**L** (0, 0.8408, 0.5414) **M** (1, 0, 0) **N** (0, 0.5414, –0.8408)	**L** (–1, 0, 0) **M** (0, 0.5761, 0.8174) **N** (0,0.8174,–0.5761)	(–0.1337, –0.4043, 0.9048)	(0,0,1)
	3	**L** (0, 0.9996, 0.0281) **M** (1, 0, 0) **N** (0,0.0281, –0.9996)	**L** (0, –0.0972, 0.9953) **M** (0, –0.9953, –0.0972) **N** (0, –0.0972, 0.9953)	(–0.0925, –0.1093, 0.9897)	(0,0,1)

[a]The GS reconstruction is adopted as that described by *Hu and Sonnerup* [2002]. See text for the detail.

been actually evaluated correctly via equations (12) and (13) (not shown here) .

[38] It should be reminded that because the magnetic field at the innermost location ($y = 0$) for the three paths is just recorded, the direction of $\hat{\mathbf{e}}_1$ and $\hat{\mathbf{n}}$ can be found accurately. If the data point at the innermost is not recorded (due to the data resolution), then a minor deviation of t_{in} would be read from $\hat{\mathbf{v}} \cdot \hat{\mathbf{b}}$ time series, and a deviation of $\hat{\mathbf{e}}_1$ would be obtained accordingly. To minimize such deviation, we suggest using the

magnetic field data of higher-resolution if available or adopting interpolation technique to yield the data of higher resolution.

4. Applications

[39] The core assumption of the new method is the cylindrical symmetry, which may be reasonable for interplanetary flux rope but may not be an evident aspect of flux rope embedding in current sheet, e.g., flux rope in magnetotail current
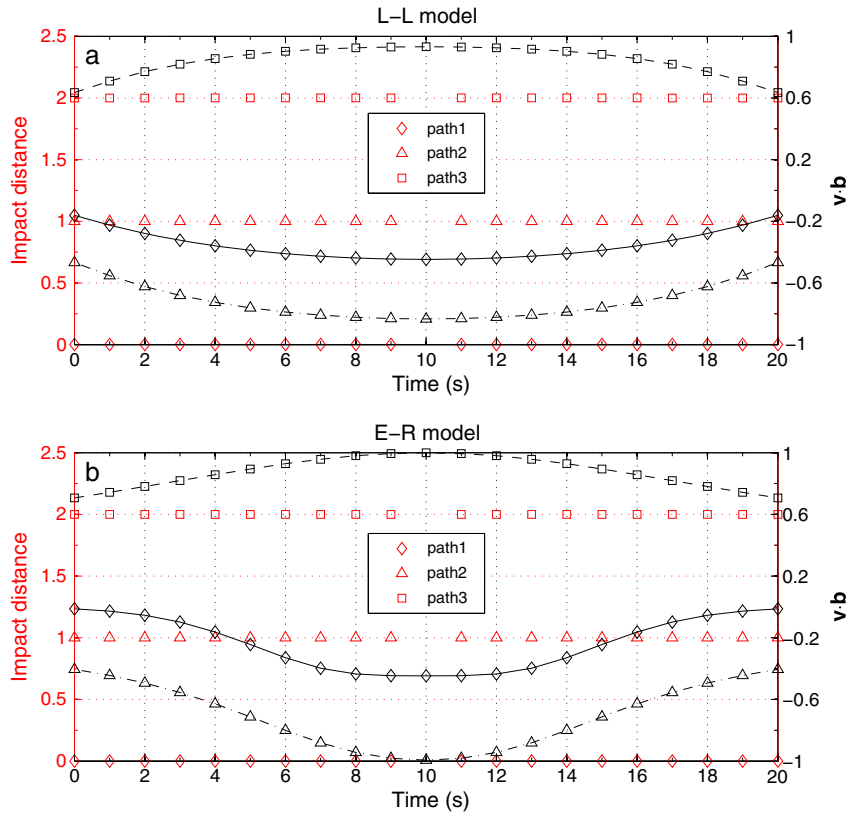
Figure 5. The time series of calculated impact distance (left *Y*-axis, red symbols) and $\hat{\mathbf{v}} \cdot \hat{\mathbf{b}}$ (right *Y*-axis, black lines with symbol) along three crossing paths for (a) L-L model and (b) E-R model.
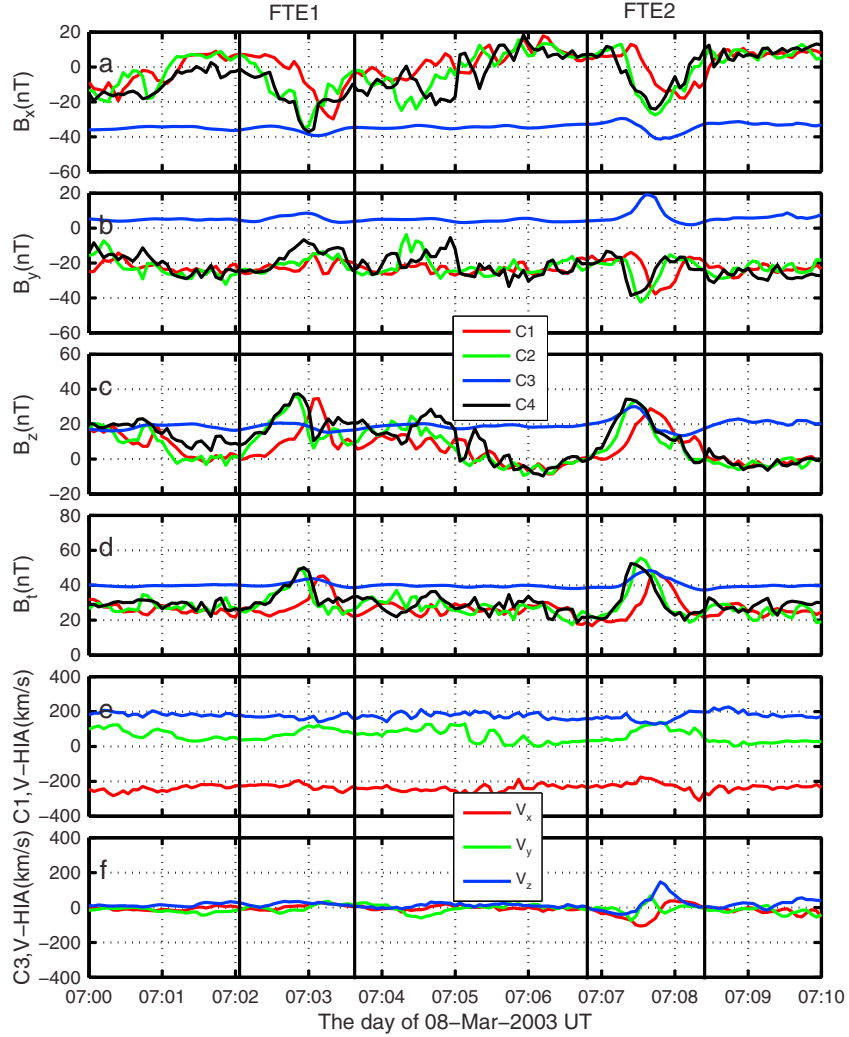
Figure 6. Cluster observation of FTEs on 8 March 2003. Panels from top to bottom show the components and the total strength of magnetic field at all 4 Cluster S/C (a–d, FGM), and the components of plasma velocity for C1 and C3 (e–f, CIS/HIA). GSE coordinates are used, and the data resolution is 4 s. The intervals for FTE1 and FTE2 are roughly marked by vertical black lines.

sheet or FTEs in magnetopause [*Kivelson and Khurana*, 1995]. The flux rope embedding in current sheet could be "pinched off" by the external lobe field, and may be plausibly described by an elliptical-like structure [e.g., *Moldwin and Hughes*, 1991; *Kivelson and Khurana*, 1995]. Due to the interaction with surrounding plasma, some studies demonstrate that the magnetic structure of flux ropes or magnetic clouds are of highly noncircular cross-sections [e.g., *Mulligan and Russell*, 2001; *Riley et al.*, 2004; *Owens and Cargill*, 2004; *Owens et al.*, 2006; *Ugai*, 2010]. Thus, the general structure of actual flux rope is believed to be noncylindrical symmetry, and it is unclear whether our method can be applied to the real case. To check this issue, in this section, we will apply the new method to an event of two successive FTEs, which were detected by the four satellites of the Cluster mission during the period of 07:00–07:10 UT on 8 March 2003. This event has been investigated previously with techniques of the optimal GS reconstruction [*Sonnerup et al.*, 2004; *Hasegawa et al.*, 2006] and the least squares of Faraday's law [*Sonnerup and Hasegawa*, 2005].

[40] During this interval, the Cluster is approximately located at [7.1, 2.5, 7.4] R_E in GSE coordinates with spacecraft separation about 5000 km. Figure 6 gives the overview of the magnetic field [*Balogh et al.*, 2001] and plasma flow data [*Reme et al.*, 2001] recorded by Cluster. The recorded intervals for FTE1 and FTE2 are marked roughly by the vertical black lines.

[41] The application requires the velocity of S/C relative to flux rope to be known and the validity of the assumption of quasi-stationary structure ($\partial/\partial t = 0$). Therefore, one has to do the DeHoffmann-Teller (HT) analysis [*Khrabrov and Sonnerup*, 1998]. Because the assumption of quasi-stationary can be checked by the HT analysis, the velocity vector V_{HT} of HT frame could be seen as the velocity of the flux rope. The quality of HT frame can be indicated by the correlation coefficient, c, between $-\mathbf{V_{HT}} \times \mathbf{B}$ and $-\mathbf{v} \times \mathbf{B}$ ($\mathbf{v}$ is the bulk plasma velocity), an acceptable quality of HT frame empirically requires $c \geq 0.9$. For this event with C1 HIA data [*Reme et al.*, 2001], *Sonnerup and Hasegawa* [2005] showed that the HT analysis gives $\mathbf{V_{HT1}} = (-226.6, 116.8,$
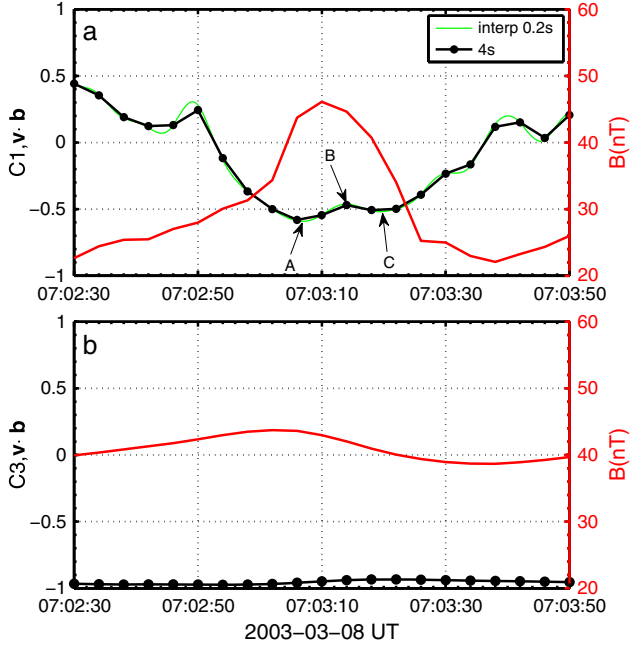
Figure 7. The time series of $\hat{\mathbf{v}} \cdot \hat{\mathbf{b}}$ (left Y-axis, black line) and magnetic field strength (right Y-axis, red line) as measured by (a) C1 and (b) C3 for FTE1. For Figure 7a, the more smooth time series of $\hat{\mathbf{v}} \cdot \hat{\mathbf{b}}$ is also shown (thin green line) with the technique of spline interpolation (0.2 s).

149.6) km/s for FTE1 (07:02:37 $\sim$ 07:03:46, $c = 0.9924$) and $\mathbf{V_{HT2}} = (-211.4, 109.6, 151.2)$ km/s for FTE2 (07:07:22 $\sim$ 07:08:27, $c = 0.9805$) in GSE with high quality. Comparing with $\mathbf{V_{HT}}$, the velocity of S/C in GSE is ignorable ($\sim$1 km/s), thus the relative velocity of S/C to FTEs can be well seen as $\mathbf{V} = -\mathbf{V_{HT}}$. In contrast, from Figure 6, the lower plasma velocity, stronger magnetic field, and the less pulse-enhanced magnetic field variation of C3 suggest that C3 locates at the side of magnetosphere and grazes FTEs. As a result, the inferred $-\mathbf{V_{HT}}$ of C3 measurement, being expectable to be much less than that of C1 (Figure 6f), cannot be seen as the velocity of the FTEs. The HIA data of C4 is unavailable during that interval. For this reason, we may assume that the three Cluster S/C are crossing the FTE with the same relative velocity, $-\mathbf{V_{HT}}$, as that derived with only C1 data.

4.1. Determining the Innermost Location

[42] Accordingly to the procedures as summarized in section 2.3, taking the measurement of C1 as an example, we will check the time series of $\hat{\mathbf{v}} \cdot \hat{\mathbf{b}}$ first for the FTE1. For the test of the above flux rope cylindrical models, the time series of $\hat{\mathbf{v}} \cdot \hat{\mathbf{b}}$ only has one extremum, which corresponds to the innermost location. However, for the crossings of true flux

rope, the yielded time series of $\hat{\mathbf{v}} \cdot \hat{\mathbf{b}}$ may have multiple extreme points, besides the one corresponding to the innermost. Evidently, as shown in Figure 7a, three extrema of $\hat{\mathbf{v}} \cdot \hat{\mathbf{b}}$ time series are present at the times A, B, and C, respectively. Thus, one has to check the three extrema one-by-one to find, which one corresponds to the innermost location. To make the time series of $\hat{\mathbf{v}} \cdot \hat{\mathbf{b}}$ more smooth, the technique of spline interpolation is adopted (time resolution 0.2 s, thin green line), so that $\hat{\mathbf{b}}_{in}$ could be estimated more accurately.

[43] To determine which extreme point corresponds to the innermost location, one has to read the corresponding $\hat{\mathbf{b}}_{in}$ and $\hat{\mathbf{e}}_1$ first from the interpolated data (0.2 s), and then take them back to the original 4 s data set to find the corresponding axis orientation. By the check of the projected $\hat{\mathbf{b}}$ on the cross-section of the corresponding inferred axis orientation, the corrected extreme point can be judged. The inferred results for the three extremes are listed in Table 2, wherein the adopted 4 s data interval of FTE 1, with a length of 36 s, is centered at each extreme point. Based on the inferred axis orientations with our new method for the three extreme points, the projection of measured unit magnetic vector, $\hat{\mathbf{b}}$, on the cross-section of the inferred axis orientations is correspondingly plotted on Figure 8. From Figure 8 and Table 2, it is clear that the axis orientation yielded from extreme B-point is reasonable, which evidently shows the loop-like structure on the cross-section with smallest residue error among the three points. Thus, we argue that the time of B-point is likely the moment when S/C is at the innermost location.

[44] From alternative perspective, the direction of field bipolar variation is along the direction of $\hat{\mathbf{e}}_1$, which is expected to be consistent with the local magnetopause normal direction. With the MVA analysis of C1 magnetic field during 06:53:11–06:55:49, the local magnetopause normal given by *Sonnerup and Hasegawa* [2005] is (0.6444, 0.2446, 0.7245) in GSE. The angles between the normal vector and the inferred $\hat{\mathbf{e}}_1$ for the three extreme points A, B, and C, are 20.0°, 8.6°, and 32.1°, respectively, which implies the B-point is more plausible to be the time when S/C are in the innermost location.

[45] One should note that the time of B-point is around the time of peak field strength (Figure 7a). Therefore, for flux ropes, the extreme points of $\hat{\mathbf{v}} \cdot \hat{\mathbf{b}}$ time series should be checked preferentially around the time of B-peak.

4.2. Results of Inferred Axis Orientations

[46] With the same procedures as done for C1, the axis orientations inferred from the other satellites measurements are obtained accordingly for both FTEs. The yielded results are listed in Table 3. However, with the C3 measurement for both FTEs, the procedures failed to yield the reasonable axis orientation for both FTEs, so the yielded results of C3

Table 2. The Inferred Axis Orientations, $\hat{\mathbf{N}}$, for the Three Extreme Points in GSE Coordinates

t_{in}[a]	Interval[b]	$\hat{\mathbf{b}}_{in}$[c]	$\hat{\mathbf{e}}_1$[c]	$\hat{N}$[c]	σ_m^2 (km²)
A: 07:03:07.0	07:02:49–07:03:25	(−0.4061, −0.3637, 0.8383)	(0.6394, 0.5423, 0.5450)	(0.0989, −0.7610, 0.6412)	1.1281×10^7
B: 07:03:14.0	07:02:56–07:03:32	(−0.5775, −0.6249, 0.5254)	(0.5906, 0.1246, 0.7973)	(−0.4296, −0.7878, 0.4413)	5.0788×10^5
C: 07:03:19.4	07:03:01–07:03:37	(−0.7979, −0.5497, 0.2474)	(0.4401, −0.2507, 0.8623)	(−0.7285, −0.6611, 0.1796)	8.9532×10^5

[a]The time of the extreme points of $\hat{\mathbf{v}} \cdot \hat{\mathbf{b}}$ time series.
[b]The adopted interval is centered at the time of tin with length being 36 s.
[c]$\hat{\mathbf{N}}$ is the inferred axis orientations (see equation (10)). Vector components are given in GSE coordinates.
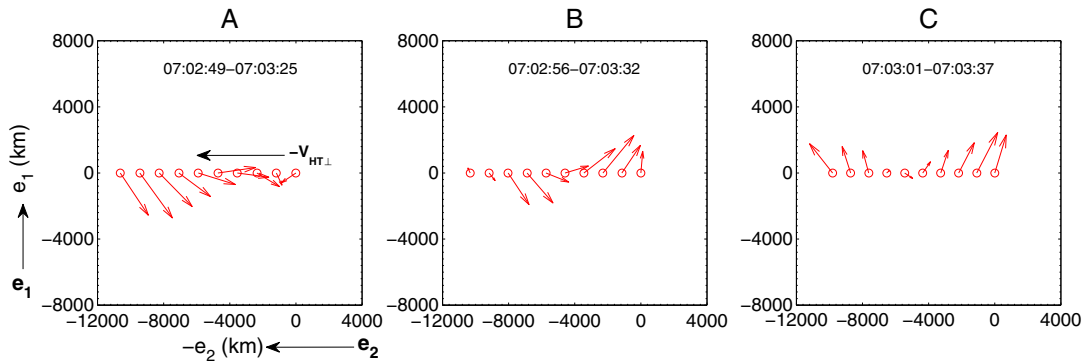
Figure 8. The projection of measured unit magnetic vector, $\hat{\mathbf{b}}$, on the cross-section of the inferred axis orientation for the three corresponding extreme points *A* (left), *B* (middle), and *C* (right) shown in Figure 7a.

are not listed in Table 3. Because the $\hat{\mathbf{v}} \cdot \hat{\mathbf{b}}$ time series of C3 is more flat (e.g., see Figure 7b for FTE1), and the impulse enhanced field strength is less than that of C1, C2, and C4 (see Figure 6d), we infer that C3 may graze both FTEs, and making the "outer" measurements, which is consistent with the following magnetic vector projection on the cross-section of inferred axis orientation (see Figure 9). As a comparison, the results yielded by the optimal GS reconstruction and the technique of Faraday's law, as quoted from *Sonnerup and Hasegawa* [2005], are also listed in Table 3. It is clear from Table 3, with our method for both FTEs, that the yielded axis orientations from the measurements of C1, C2, and C4 are basically the same as that yielded from optimal GS reconstruction and the technique of Faraday's law. Meanwhile, for measurements from each S/C, the yielded residue error of the impact distance, σ_m, is evidently less than the average impact distance, which means the assumption of cylindrical symmetry is valid and acceptable for the crossings of C1, C2, and C4.

4.3. Implications of Results

[47] Figure 9 shows the projection of unit magnetic vector, $\hat{\mathbf{b}}$, measured by the four S/C in the path, on the cross-section of each inferred axis orientation. Obviously, the loop-like field structure on the cross-section can be reasonably found

via our single-point method for the measurements of C1, C2, and C4, which demonstrates that our method is basically reasonable and applicable. In contrast, our method fails for the measurements of C3, which is just grazing the FTEs. Therefore, at least for this case, it seems that the cylindrical symmetry is still an acceptable assumption for the inner field structure of flux rope (detected by C1, C2, and C4) as being less affected by the external field.

[48] It should be cautioned that for both FTEs, although the detected magnetic vector in the path can be well approximated by the cylindrical symmetric structure seen along the yielded axis orientation, one still cannot ensure that the whole structure of flux rope has a cylindrical symmetry. Two related aspects should be noted. First, because the shape of Cluster tetrahedron can be assumed to be unvaried during the transient FTE crossings, the yielded directions of $\hat{\mathbf{e}}_1$ for all the S/C should be the same if the FTEs are of ideal cylindrical symmetry. In contrast to FTE1, the yielded directions of $\hat{\mathbf{e}}_1$ from the three S/C for FTE2 are almost the same (see Table 3), which implies that the structure of FTE2 is closer to the cylindrical symmetry. Consistently, the yielded axis orientations from the three S/C for FTE2 are more similar than that of FTE1. Our results for FTE2 are also in good agreement with the ones that are derived from the optimal GS reconstruction and the technique of Faraday's law.

Table 3. Comparison of Results From Different S/C With the New Method in GSE Coordinates

S/C	t_{in}[a]	Interval[b]	$\hat{\mathbf{e}}_1$[c]	$\hat{\mathbf{N}}$[c]	$<r_0>$ (km)	σ_m (km)
			FTE1			
C1	07:03:14.0	07:02:56~07:03:32	(0.5906, 0.1246, 0.7973)	(−0.4296, −0.7878, 0.4413)	1987	713
C2	07:02:56.6	07:02:38~07:03:14	(0.5673, 0.0475, 0.8222)	(−0.6685, −0.5566, 0.4934)	665	587
C4	07:02:56.0	07:02:38~07:03:14	(0.6331, 0.3340, 0.6983)	(−0.5441, −0.4496, 0.7084)	1914	1018
Multi-GS[d]	-	07:02:37 ~ 07:03:46	(0.6186, 0.2439, 0.7467)	(−0.4732, −0.6430, 0.6021)	-	-
Faraday law, C1[d]	-	07:02:37 ~ 07:03:46	(0.6238, 0.2793, 0.7299)	(−0.4568, −0.6051, 0.6521)	-	-
			FTE2			
C1	07:07:51.2	07:07:33 ~ 07:08:09	(0.6453, 0.2477, 0.7227)	(−0.3427, −0.7516, 0.5636)	1644	794
C2	07:07:32.6	07:07:14 ~ 07:07:50	(0.6459, 0.2513, 0.7209)	(−0.2587, −0.8164,0.5164)	1941	906
C4	07:07:32.4	07:07:14 ~ 07:07:50	(0.6551, 0.3187, 0.6850)	(−0.3298, −0.6951, 0.6388)	1692	1129
Multi-GS[d]	-	07:07:22 ~ 07:08:27	(0.6488, 0.2695, 0.7117)[d]	(−0.3296, −0.7434, 0.5820)	-	-
Faraday law, C1[d]	-	07:07:22 ~ 07:08:27	(0.6404, 0.2237, 0.7348)[d]	(−0.3698, −0.7212, 0.5857)	-	-

[a]The time when S/C located in the innermost of FTEs.
[b]The adopted interval is centered at the time of tin with length being 36 s.
[c]The inferred axis orientations (see equation (10)). Vector components are given in GSE coordinates.
[d]The results of both FTEs are quoted from *Sonnerup and Hasegawa* [2005], wherein $\hat{\mathbf{e}}_1 = \frac{\hat{N} \times V}{|\hat{N} \times V|}$, and $\mathbf{V} = -\mathbf{V}_{HT}$.
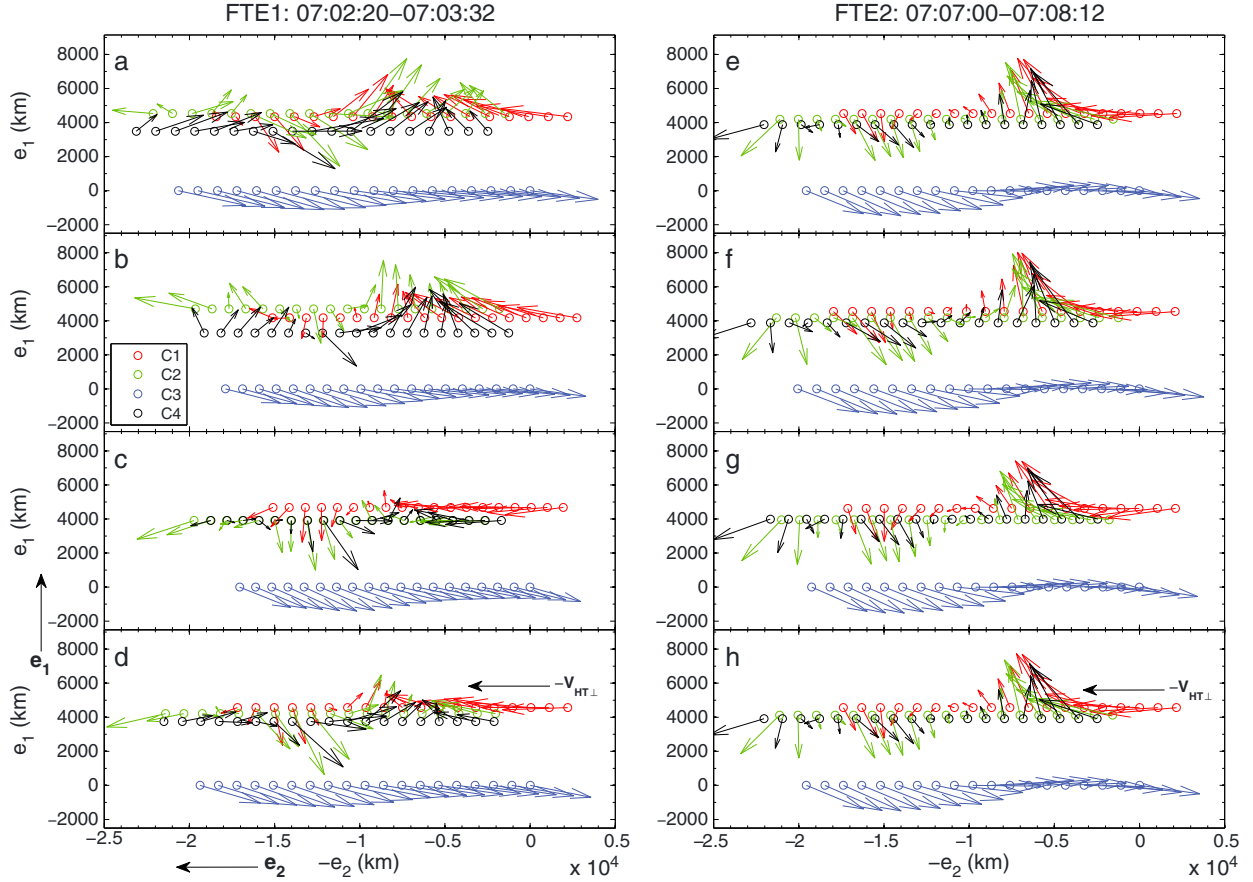
Figure 9. For both FTEs, the projection of $\hat{\mathbf{b}}$, measured by the four S/C in the path, on the cross-section of each axis orientation, which is inferred only by the measurements of C1 (a and e), C2 (b and f), and C4 (c and g), respectively, and that inferred by the optimal GS reconstruction with multi-S/C measurements (d and h, see Table 3). The measurements of C1, C2, C3, and C4 are labeled as the red, green, blue, and black colors, respectively.

Second, not all the yielded axis orientations from the three S/C are strictly reasonable. Taking Figure 9b for FTE1 as an example, the spatial variation of C2's magnetic vector indicates that the axis is above (in the direction of $\hat{\mathbf{e}}_1$) the C2's path, whereas the variation of C1's magnetic vector indicates C1's path is basically crossing the axis that is below the C2's path. The main reason might be that the structure of FTE1 is not the ideal cylindrical symmetry. Therefore, considering the complicated structure of actual flux rope, the more accurate axis orientation should be self-consistently yielded by the multipoint observation if the multipoint measurements are available, and our method needs further update for the multipoint measurements.

5. Summary and Discussion

[49] In this study, we present a new method to infer the axis orientation of cylindrical flux rope based on single-point analysis of magnetic field structure. The tests of two classic cylindrical models demonstrate that our method can consistently yield the axis orientation for any crossing path comparable to the techniques of BMVA, bMVA, and

GS reconstruction. In addition, the method has the ability to evaluate the local radial distance and the current density (see equations (12)–(13)). The application to an event of two successive FTEs demonstrates that the method is more appropriate to be used for the inner part of the flux rope, which might be closer to the cylindrical structure, but fails for the measurement of the outer part/boundary field, as any other present method. For further applications, several points should be noted as follows:

1. Checking of $\hat{\mathbf{v}}\cdot\hat{\mathbf{b}}$ time series is necessary. Generally, data series obeys the order: external field-boundary/outer field-inner field for entering into flux rope, and the reverse order for exiting from the flux rope. Because the external field is generally uniform, the time series of $\hat{\mathbf{v}}\cdot\hat{\mathbf{b}}$ should be valley-like or peak-like (e.g., Figure 7). Thus, by the check of $\hat{\mathbf{v}}\cdot\hat{\mathbf{b}}$ time series, one could first judge whether a detected magnetic structure belongs to the flux rope category before the analysis. On the other hand, if the multipoint measurements are available, for the S/C crossing the inner part of flux rope, the yielded $\hat{\mathbf{v}}\cdot\hat{\mathbf{b}}$ time series is changing more significantly than that

of S/C grazing flux rope (see Figure 7b). Thus, with comparison of multipoint measurements, the check of $\hat{\mathbf{v}}\cdot\hat{\mathbf{b}}$ could also help to evaluate the distance of S/C to the axis center roughly.

2. As we have shown in the applied study, for the actual flux rope crossing, the time series of $\hat{\mathbf{v}}\cdot\hat{\mathbf{b}}$ may have multiple extreme points. Therefore, one should be careful to determine, which extreme point corresponds to the innermost location. The best way is to check these extreme points one-by-one as we do for the C1 measurements of FTE1. For flux ropes, the extreme points of $\hat{\mathbf{v}}\cdot\hat{\mathbf{b}}$ around the time of B-peak should be checked preferentially. Moreover, for a flux rope embedded in a current sheet, if the normal of current sheet is available, one may get the quick judgment of the reliability of an extremum point by comparing the direction of $\hat{\mathbf{v}}\times\hat{\mathbf{b}}_{\mathrm{in}}$ to the normal.

3. It should be reminded that our method tries to find an axis orientation of flux rope, along which the detected magnetic vector in the path can be well constructed by a cylindrical symmetry structure. However, the actual structure of flux rope is complicated and generally believed to have noncylindrical symmetry, thus it should be applied with caution. The studied cases demonstrate that, for the actual applications, the assumption of cylindrical symmetry might be acceptable for the inner field of observed flux ropes, but violated for the outer/boundary field.

4. With the minimum residue error σ_{m}, a dimensionless parameter $|\sigma_{\mathrm{m}}|/\langle r_0\rangle$ is constructed as an indicator for the quality of cylindrical symmetry assumption. The smaller the parameter, the better is the assumption of cylindrical symmetry.

5. Due to interaction with surrounding plasma, the field structure near boundaries of flux ropes may deviate from the cylindrical structure evidently. Using our method, the boundaries of flux ropes can be also evaluated. Because the impact distance r_{0i} can be derived from equation (5), if the studied interval including boundaries, a systematic trend near the boundary is to be expected in r_{0i} when plotted versus time. In the same way, if the flux rope is significantly noncircular, a systematic trend is also to be expected in r_{0i} versus time inside the flux rope region. Then plotting r_{0i} versus time looks to be important to control both the locations of the boundaries and the circularity of the analyzed event. If r_{0i} versus time shows a significant trend near a boundary, the time interval can be accordingly reduced, then σ^2 minimized again, then r_{0i} versus time checked again. In the reverse way, the time interval can be increased up to the detection of a trend near the boundaries. Therefore, with a very limited number of iterations, the flux rope region can be determined from our method. Then, the deduced boundaries can be compared to traditional ways of determining them.

6. When S/C is nearly passing orthogonally to the flux rope, e.g., along Y-axis with impact distance, x (see path 3 in Figure 3), if $b_\perp$ has an almost linear dependence with the radial distance, r, in the path, then we would have $\hat{\mathbf{v}}\cdot\hat{\mathbf{b}} = \mathbf{v}_y\mathbf{b}_\perp\dfrac{x}{r}$, which almost keeps constant. Therefore, it would be not so easy to find t_{in} by checking the rather

flat time series $\hat{\mathbf{v}}\cdot\hat{\mathbf{b}}$. Therefore, our method would fail for such special case. Nonetheless, such case is special, and so unlikely to occur.

7. We may generalize the axis orientation in equations (4)–(9) as a function of two independent variable angles, i.e., $\hat{\mathbf{n}}(\theta_1,\theta_2)$. Considering the neighboring measurements, the impact distance at time t_i can also be evaluated from equation (5) as $r_{0i} = \dfrac{L_{i+1} \pm L_i}{\tan\phi_{i+1} \pm \tan\phi_i} \sim \dfrac{V_\perp \Delta t}{\Delta\phi_i}$ where, Δt is the neighboring interval, $\Delta\phi$ is the angle between the neighboring $b_\perp$. Therefore, a residue equation as a function of θ_1,θ_2 can be constructed accordingly. Then, through numerical adjustment of $\hat{\mathbf{n}}(\theta_1,\theta_2)$ making residue function $\sigma^2(\theta_1,\theta_2)$ minimum, the final axis orientation can be found. Although the $\hat{\mathbf{v}}\cdot\hat{\mathbf{b}}$ extremum can be avoided to be read from the much flat series, much more calculation would be involved in the generalization. The generalization needs to be detailed more in future studies.

8. It should be noted that when the S/C is crossing a flux rope of strictly elliptical cross-section along its semi-major or semi-minor axis directions, our method still has the ability to yield a consistent axis orientation. Given a strictly elliptical flux rope whose cross-section satisfying $\dfrac{x^2}{a^2}+\dfrac{y^2}{b^2}=1$, S/C is crossing the flux rope with trajectory projected in x-y plane being along the x-direction. The detected perpendicular magnetic vector $\hat{\mathbf{b}}_{i\perp}$ at time t_i contains b_{ix} and b_{iy} components. If we take $X=x$, $Y=\dfrac{a}{b}y$, the elliptic flux rope can be transformed to be a cylindrical type, and $b_{iX}=b_{ix}$, $b_{iY}=\dfrac{a}{b}b_{iy}$. The term $\tan\phi_i$ in equation (5), thus, becomes $\tan\phi_i = \dfrac{b_{iy}}{b_{ix}} = \dfrac{b}{a}\dfrac{b_{iy}}{b_{ix}} = \dfrac{b}{a}\tan\Phi_i$, and the impact distance can be derived as $r_{0i}=\dfrac{a}{b}\dfrac{L_i}{\tan\Phi_i}$ Because the term $\dfrac{L_i}{\tan\Phi_i}$ is actually the impact distance for the transformed cylindrical type, the obtained time series of impact distance r_{0i} for the elliptical flue rope should keep constant, which guarantees the validity of our method.

9. Finally, the assessment of the method accuracy needs further analysis before applying it broadly to observations, although the application to an event of both FTEs demonstrates that our method is reasonable and applicable.

Reference

Balogh, A., et al. (2001), The Cluster magnetic field investigation: Overview of inflight performance and initial results, *Ann. Geophys.*, *19*, 1207–1218.

Burlaga, L. F. (1988), Magnetic Clouds and Force-Free Fields with Constant Alpha, *J. Geophys. Res.*, *93*(A7), 7217–7224, doi:10.1029/JA093iA07p07217.

Burlaga, L. F., R. P. Lepping, and J. A. Jones (1990), Global configuration of a magnetic cloud, in Physics of Magnetic Flux Ropes, Geophys. Monogr. Ser., vol. *58*, edited by C. T. Russel, E. R. Priest, and L. C. Lee, pp. 373–377, AGU, Washington, D. C.

Elphic, R. C., and C. T. Russell (1983), Magnetic Flux Ropes in the Venus Ionosphere: Observations and Models, *J. Geophys. Res.*, *88*(A1), 58–72, doi:10.1029/JA088i01p00058.

Gekelman, W., E. Lawrence, and B. Van Compernolle (2012), Three-dimensional Reconnection Involving Magnetic Flux Ropes, *ApJ*, *753*, 131–146, doi:10.1088/0004-637X/753/2/131.

Gulisano, A. M., S. Dasso, C. H. Mandrini, and P. Démoulin (2007), Estimation of the bias of the Minimum Variance technique in the determination of magnetic clouds global quantities and orientation, *Adv. Space Res.*, *40*, 1881–1890.

Hasegawa, H., B. U. Ö. Sonnerup, B. Klecker, G. Paschmann, M. W. Dunlop, and H. Rème (2005), Optimal reconstruction of magnetopause structures from Cluster data, *Ann. Geophys.*, *23*, 973–982.

Hasegawa, H., B. U. Ö. Sonnerup, C. J. Owen, B. Klecker, G. Paschmann, A. Balogh, and H. Rème (2006), The structure of flux transfer events recovered from Cluster data, *Ann. Geophys.*, *24*, 603–618.

Hau, L.-N., and B. U. Ö. Sonnerup (1999), Two-dimensional coherent structures in the magnetopause: Recovery of static equilibria from single-spacecraft data, *J. Geophys. Res.*, *104*(A4), 6899–6917, doi:10.1029/1999JA900002.

Hones, E. W., Jr. (1977), Substorm processes in the magnetotail: Comments on"On hot tenuous plasma, fireballs, and boundary layers in the Earth's magnetotail" by L.A. Frank et al., *J. Geophys. Res.*, *82*, 5633.

Hones, E. W., Jr., J. Birn, S. J. Bame, G. Paschmann, and C. T. Russell (1982), On the three-dimensional magnetic structure of the plasmoid created in the magnetotail at substorm onset, *Geophys. Res. Lett.*, *9*(3), 203–206, doi:10.1029/GL009i003p00203.

Hu, Q., and B. U. Ö. Sonnerup (2002), Reconstruction of magnetic clouds in the solar wind: Orientations and configurations, *J. Geophys. Res.*, *107*(A7), 1142, doi:10.1029/2001JA000293.

Hughes, W. J., and D. Sibeck (1987): On the 3-dimensional structure of plasmoid, *Geophys. Res. Lett.*, *14*, 636–639.

Khrabrov, A. V., and B. U. Ö. Sonnerup (1998), DeHoffmann-Teller Analysis, in Analysis Methods for Multi-Spacecraft Data, edited by G. Paschmann and P. W. Daly, pp. 221–248, Eur. Space Agency, Noordwijk, Netherlands.

Kivelson, M. G., and K. K. Khurana (1995), Models of Flux Ropes Embedded in a Harris Neutral Sheet: Force-Free Solutions in Low and High Beta Plasmas, *J. Geophys. Res.*, *100*(A12), 23,637–23,645, doi:10.1029/95JA01548.

Lee, L. C. (1995), A Review of Magnetic Reconnection: MHD Models, in Physics of the Magnetopause, Geophys. Monogr. Ser., vol. *90*, edited by P. Song, B. U. Ö. Sonnerup, and M. F. Thomsen, p. 139–153, AGU, Washington, D. C.

Lepping, R., J. Jones, and L. Burlaga (1990), Magnetic Field Structure of Interplanetary Magnetic Clouds at 1 AU, *J. Geophys. Res.*, *95*(A8), 11957–11965.

Li, H. J., X. S. Feng, P. B. Zuo, and Y. Q. Xie (2009), Inferring interplanetary flux rope orientation with the minimum residue method, *J. Geophys. Res.*, *114*, A03102, doi:10.1029/2008JA013331.

Lin, J., S. R. Cranmer, and C. J. Farrugia (2008), Plasmoids in reconnecting current sheets: Solar and terrestrial contexts compared, *J. Geophys. Res.*, *113*, A11107, doi:10.1029/2008JA013409.

Lockwood, M., and M. A. Hapgood (1998), On the cause of a magnetospheric flux transfer event, *J. Geophys. Res.*, *103*(A11), 26,453–26,478, doi:10.1029/98JA02244.

Lundquist, S. (1950), Magneto-hydrostatic fields, *Ark. Fys.*, *2*, 316–365.

Lui, A. T. Y., M. W. Dunlop, H. Rème, L. M. Kistler, G. Gustafsson, and Q.-G. Zong (2007), Internal structure of a magnetic flux rope from Cluster observations, *Geophys. Res. Lett.*, *34*, L07102, doi:10.1029/2007GL029263.

Moldwin, M. B., and W. J. Hughes (1991), Plasmoids as magnetic flux ropes, *J. Geophys. Res.*, *96*, 14,051.

Moldwin, M. B., and W. J. Hughes (1993), Geomagnetic Substorm Association of Plasmoids, *J. Geophys. Res.*, *98*(A1), 81–88, doi:10.1029/92JA02153.

Mulligan, T., and C. T. Russell (2001), Mulitspacecraft modeling of the flux rope structure of interplanetary coronal mass ejections: Cylindrical symmetric versus nonsymmetric topologies, *J. Geophys. Res.*, *106*, 10,581.

Nagai, T., K. Takahashi, H. Kawano, T. Yamamoto, S. Kokubun, and A. Nishida (1994), Initial GEOTAIL survey of magnetic substorm signatures in the magnetotail, *Geophys. Res. Lett.*, *21*(25), 2991–2994, doi:10.1029/94GL01420.

Owens, M. J., and P. J. Cargill (2004), Non-radial solar wind flows induced by the motion of interplanetary coronal mass ejections, *Ann. Geophys.*, *22*, 4397.

Owens, M. J., V. G. Merkin, and P. Riley (2006), A kinematically distorted flux rope model for magnetic clouds, *J. Geophys. Res.*, *111*, A03104, doi:10.1029/2005JA011460.

Pu, Z. Y., et al. (2004), Multiple flux rope events at the high-latitude magnetopause: Cluster/Rapid observation on January 26, 2001, *Surv. Geophys.*, *26*(1-3), 193–214.

Rème, H., et al. (2001), First multispacecraft ion measurements in and near the Earth's magnetosphere with the identical Cluster Ion Spectrometry (CIS) experiment, *Ann. Geophys.*, *19*, 1303–1354, doi:10.5194/angeo-19-1303-2001.

Riley, P., J. A. Linker, R. Lionello, Z. Mikic, D. Odstre`il, M. A. Hidalgo, Q. Hu, R. P. Lepping, B. J. Lynch, and A. Rees (2004), Fitting flux-ropes to a global MHD solution: A comparison of techniques, *J. Atmos. Sol. Terr. Phys.*, *66*, 1321.

Russell, C. T., and R. C. Elphic (1979a), ISEE observations of flux transfer events at the dayside magnetopause, *Geophys. Res. Lett.*, *6*(1), 33–36, doi:10.1029/GL006i001p00033.

Russell, C. T., and R. C. Elphic (1979b), Observation of magnetic flux ropes in the Venus ionosphere, *Nature*, *279*, 616–618.

Russell, C. T. (1990), Magnetic flux ropes in the ionosphere of Venus, in Physics of Magnetic Flux Ropes, Geophys. Monogr. Ser., vol. *58*, edited by C. T. Russell, E. R. Priest, and L. C. Lee, p. 413–423, AGU, Washington, D. C.

Shen, C., et al. (2007), Magnetic field rotation analysis and the applications, *J. Geophys. Res.*, *112*, A06211, doi:10.1029/2005JA011584.

Shi, Q. Q., C. Shen, Z. Y. Pu, M. W. Dunlop, Q.-G. Zong, H. Zhang, C. J. Xiao, Z. X. Liu, and A. Balogh (2005), Dimensional analysis of observed structures using multipoint magnetic field measurements: Application to Cluster, *Geophys. Res. Lett.*, *32*, L12105, doi:10.1029/2005GL022454.

Schindler, K. (1974), A theory of the substorm mechanism, *J. Geophys. Res.*, *79*(19), 2803–2810, doi:10.1029/JA079i019p02803.

Slavin, J. A., et al. (2003), Cluster electric current density measurements within a magnetic flux rope in the plasma sheet, *Geophys. Res. Lett.*, *30*(7), 1362, doi:10.1029/2002GL016411.

Slavin, J. A., et al. (2009), MESSENGER observations of magnetic reconnection in Mercury's magnetosphere, *Science*, *324*, 606–610, doi:10.1126/science.1172011.

Sonnerup, B., and L. Cahill Jr. (1968), Explorer 12 Observations of the Magnetopause Current Layer, *J. Geophys. Res.*, *73*(5), 1757–1770.

Sonnerup, B. U. Ö., H. Hasegawa, and G. Paschmann (2004), Anatomy of a flux transfer event seen by Cluster, *Geophys. Res. Lett.*, *31*, L11803, doi:10.1029/2004GL020134.

Sonnerup, B. U. Ö., and H. Hasegawa (2005), Orientation and motion of two-dimensional structures in a space plasma, *J. Geophys. Res.*, *110*, A06208, doi:10.1029/2004JA010853

Ugai, M. (2010), Magnetic field structure of large-scale plasmoid generated by the fast reconnection mechanism in a sheared current sheet, *Ann. Geophys.*, *28*, 1511–1521, 2010.

Vignes, D., M. H. Acuña, J. E. P. Connerney, D. H. Crider, H. Rème, and C. Mazelle (2004), Magnetic flux ropes in the Martian atmosphere: Global characteristics, *Space Sci. Rev. 111*(1-2), 223–231.

Wang, Y. M., S. Wang, and P. Z. Ye (2002), Multiple magnetic clouds in interplanetary space, *Sol. Phys.*, *211*, 333–344, doi:10.1023/A:1022404425398.

Wang, Y. M., P. Z. Ye, and S. Wang (2003), Multiple magnetic clouds: Several examples during March –April 2001, *J. Geophys. Res.*, *108*(A10), 1370, doi:10.1029/2003JA009850.

Wei, H. Y., C. T. Russell, T. L. Zhang, and M. K. Dougherty (2010), Comparison study of magnetic flux ropes in the ionospheres of Venus, *Mars and Titan, Icarus*, *206*,174–181.

Xiao, C. J., et al. (2004), Inferring of flux rope orientation with the minimum variance analysis technique, *J. Geophys. Res.*, *109*, A11218, doi:10.1029/2004JA010594.

Zhang, T. L., et al. (2012), Magnetic Reconnection in the Near Venusian Magnetotail, *Science*, doi:10.1126/science.1217013.

Zhang, Y. C., Z. X. Liu, C. Shen, A. Fazakerley, M. Dunlop, E. Lucek, A. P. Walsh, and L. Yao (2007), The magnetic structure of an earthward-moving flux rope observed by cluster in the near-tail, *Ann. Geophys.*, *25*, 1471–1476.

Zhang, H., et al. (2008), Modeling a force-free flux transfer event probed by multiple Time History of Events and Macroscale Interactions during Substorms (THEMIS) spacecraft, *J. Geophys. Res.*, *113*, A00C05, doi:10.1029/2008JA013451.

Zhou, X.-Z., et al. (2006), Multiple Triangulation Analysis: another approach to determine the orientation of magnetic flux ropes, *Ann. Geophys.*, *24*, 1759–1765.

Zong, Q.-G., et al. (1997), Geotail observations of energetic ion species and magnetic field in plasmoid-like structures in the course of an isolated substorm event, *J. Geophys. Res.*, *102*(A6), 11,409–11,428, doi:10.1029/97JA00076.

Zong, Q.-G., et al. (2003), Bursty energetic electrons confined in flux ropes in the cusp region, *Planet. Space Sci.*, *51*(12), 821–830.

Zong, Q.-G., et al. (2004), Cluster observations of earthward flowing plasmoid in the tail, *Geophys. Res. Lett.*, *31*, L18803, doi:10.1029/2004GL020692.